

Understanding Degradation Mechanisms in Water-In-Salt Electrolyte. Part 2: Impact of the Electrochemical Parameters on the Cycling Behavior of LiFePO₄ versus TiS₂

Célia Doublet, Théo Faverge, Vincent Martin, Hiram Castillo Michel, Jean-Pascal Rueff, Marian Chatenet, Lauréline Lecarme, and Claire Villevieille*

Water-in-salt electrolytes (WiSE) have emerged as a promising route for the development of safe and high-voltage aqueous lithium-ion batteries, owing to their expanded electrochemical stability window (ESW) and reduced safety issue. Despite this potential, the long-term cycling performance of WiSE-based cells remains hindered by multiple degradation phenomena all related to water, including hydrogen and oxygen evolution reactions, carbon corrosion, and interfacial instabilities. In this study, the electrochemical behavior and degradation mechanisms of full cells based on LiFePO₄ and TiS₂ electrodes are systematically investigated in 21 m LiTFSI electrolyte. Gas evolution is quantified

using online electrochemical mass spectrometry (OEMS), while surface chemistry and morphology were analyzed via X-ray photoelectron spectroscopy (XPS), scanning electron microscopy (SEM), and synchrotron-based hard X-ray photoelectron spectroscopy (HAXPES). The results demonstrate that both electrode materials undergo significant parasitic reactions—even within the ESW—leading to the formation of a LiF-rich but unstable solid electrolyte interphase and progressive accumulation of salt decomposition products. The degradation is further influenced by electrochemical parameters such as C-rate, electrode balancing, and voltage window.

1. Introduction

Water-in-salt (WiSE) electrolytes have attracted significant attention as a promising route for safe and high-voltage aqueous lithium-ion batteries.^[1] These systems combine the intrinsic safety benefits of aqueous electrolytes with an expanded electrochemical stability window (ESW), exceeding 3 V, compared to the thermodynamic 1.23 V limit of pure water.^[2]

Suo et al.^[3] demonstrated the feasibility of WiSE electrolytes by assembling a full cell operating at 2.3 V, employing Mo₆S₈ and

LiMn₂O₄ as the negative and positive electrodes, respectively, with a 21 m LiTFSI electrolyte. This cell exhibited remarkable cycling stability, achieving over 1000 cycles at a high rate of 4.5C with satisfactory coulombic efficiency. Subsequently, the same group investigated LiFePO₄ as a positive electrode material in conjunction with Mo₆S₈ and the same 21 m LiTFSI electrolyte.^[4] This configuration exhibited improved cycle life (1000 cycles at 1C rate) but operated at a reduced voltage of 1.3 V compared to the LiMn₂O₄/Mo₆S₈ system, leading to poor energy improvement. In an effort to further increase the cell voltage and leverage the full ESW of the electrolyte, Wang et al.^[5] employed LiNi_{0.5}Mn_{1.5}O₄ as the positive electrode material, again paired with Mo₆S₈. This system achieved a cell voltage of 2.9 V and sustained 400 cycles at a 5C rate using a mixed 21 m LiTFSI + 1 m HTFSI electrolyte. Alternative negative electrode materials have also been evaluated. Sun et al.^[6] reported a LiMn₂O₄/TiS₂ full cell with a working voltage of 1.7 V and a limited cycle life of 50 cycles at 1C rate. The relatively low coulombic efficiency (<97%) suggested the occurrence of parasitic reactions, likely responsible for the observed capacity fade, though no further mechanistic analysis was conducted. Kidanu et al.^[7] studied the LiFePO₄/TiS₂ couple and optimized electrochemical parameters to improve capacity retention. By adjusting the cut-off voltage to 1.6 V, they extended the cycle life to 50 cycles at C/2 rate, although substantial capacity degradation remained visible.

Interestingly, most studies on WiSE batteries have been conducted at relatively high cycling rates, which appear to mitigate some side effects. Nonetheless, the long-term electrochemical performance of WiSE systems remains hindered by several degradation mechanisms. Among these, the hydrogen evolution

C. Doublet, T. Faverge, V. Martin, M. Chatenet, L. Lecarme, C. Villevieille
Université Grenoble Alpes, Université Savoie Mont Blanc,
CNRS, Grenoble, INP, LEPMI
Grenoble 38000, France
E-mail: claire.villevieille@grenoble-inp.fr, claire.villevieille@gmail.com

H. C. Michel
European Synchrotron Radiation Facility
71 Av. des Martyrs, Grenoble 38000, France

J.-P. Rueff
SOLEIL Synchrotron
L'Orme des Merisiers
Départementale 128, Saint-Aubin 91190, France

J.-P. Rueff
Sorbonne Université,
CNRS, Laboratoire de Chimie Physique—Matière et Rayonnement LCPMR
Paris 75005, France

 Supporting information for this article is available on the WWW under <https://doi.org/10.1002/batt.202500678>

 © 2025 The Author(s). *Batteries & Supercaps* published by Wiley-VCH GmbH. This is an open access article under the terms of the Creative Commons Attribution License, which permits use, distribution and reproduction in any medium, provided the original work is properly cited.

reaction (HER) and oxygen evolution reaction (OER), arising from residual water activity, are frequently pointed out despite the high salt concentrations designed to suppress such processes. Surprisingly, degradation phenomena often persist even when the electrodes operate within the expected ESW, meaning that degradation pathways are still unclear to date.

For instance, Droguet et al.^[8] reported a decrease in coulombic efficiency at lower C-rates in LiFePO₄/Mo₆S₈ full cells utilizing 20 m LiTFSI. Through *in situ* gas analysis, they identified HER occurring between 1.0 and 1.5 V, with a strong activity near 1.4 V—well above the theoretical limit—underscoring the complexity of stability in concentrated aqueous systems. Potential origins of this behavior include: (i) incomplete or unstable solid electrolyte interphase (SEI) formation,^[9] (ii) local pH fluctuations affecting ESW limits, and/or (iii) measurement artifacts related to the choice of reference electrode.

To elucidate the nature and reversibility of SEI passivation, SEI formation was mimicked on glassy carbon electrodes via successive cyclic voltammetry (CV) scans at 50 mV s⁻¹. After 15 cycles, HER signals were nearly suppressed, indicating effective surface passivation. However, after a one-hour OCV hold, the HER peak re-emerged, suggesting SEI dissolution or degradation. Similar observations were made by Jommongkol et al.^[10] via *operando* optical imaging, further confirming SEI instability in aqueous environments.^[10] In a subsequent study, Droguet et al.^[11] quantitatively monitored water consumption linked to HER as a function of SEI formation in LiMn₂O₄/Mo₆S₈ full cells. Their findings indicated that prolonged or repeated SEI formation reduced water loss during self-discharge. Nonetheless, HER could not be entirely stopped, even after extensive SEI formation, pointing to the insufficient passivating capability of this interphase. This persistent water consumption ultimately increases the salt concentration of the electrolyte, potentially leading to salt precipitation and cell dry-out. Moreover, other parasitic processes, such as corrosion, are suspected to play a key role in the end-of-life mechanisms of WISE cells and warrant further investigation.

In the Part 1 of this study, we conducted a systematic investigation of the chemical and structural stability of electrode materials (LiFePO₄ and TiS₂) upon prolonged exposure to WISE electrolytes, during soaking process. We demonstrated that LiFePO₄ remains structurally stable after electrolyte soaking, whereas TiS₂ undergoes significant surface alteration, including partial conversion to TiO₂. In both cases, a native SEI layer enriched in LiF was detected.

Based on these findings, we carried out a comprehensive electrochemical study of LiFePO₄ versus TiS₂ full cells in water-in-salt electrolytes (WISE) to unravel the degradation pathways as a function of electrochemical activity. In particular, we employed online electrochemical mass spectrometry (OEMS) to monitor gas evolution during cycling and identify HER and OER signatures. These results were correlated with *ex situ* X-ray photoelectron spectroscopy (XPS) and postmortem SEM to characterize surface chemistry of both electrode materials after cycling. Finally, we evaluated the impact of electrochemical parameters—including cycling rate, electrode balancing, and cut-off voltages—to

establish optimal cycling conditions and gain deeper insights into failure mechanisms in WISE systems.

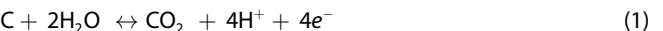
2. Gas Evolution of Both Electroactive Materials

Before assessing the electrochemical performance of LiFePO₄ versus TiS₂ full cells in WISE, we conducted a thorough investigation of gas evolution during cycling using an OEMS setup (Figure S1, Supporting Information). This analysis aimed to determine the onset potentials of the HER and OER, thereby shedding light on potential parasitic reactions occurring during operation. As shown in Figure S2 (Supporting Information), both electrode materials—LiFePO₄ and TiS₂—operate within the ESW of the 21 m LiTFSI electrolyte. Therefore, under ideal cycling conditions, neither HER nor OER should be detected by OEMS measurements.

2.1. Case of LiFePO₄ Electrode Material

The electrochemical behavior of LiFePO₄ was evaluated by CV at a scan rate of 1 mV s⁻¹ over ten consecutive cycles (Figure S3, Supporting Information). The initial CV cycle was performed between 4.9 and 1.85 V versus Li⁺/Li and revealed the signs of parasitic reactions, as evidenced by the evolution of O₂ at high potential and H₂ at low potential, as shown in Figure 1. Specifically, O₂ evolution was observed at ≈4.75 V versus Li⁺/Li, and H₂ at around 2.5 V versus Li⁺/Li—both deviating from the theoretical values expected for the OER and HER. These discrepancies can be attributed to differences in electrode morphology: while the ESW of the electrolyte is typically measured using smooth, inert metal model electrodes, the composite electrodes used here possess significantly larger surface areas, which can markedly influence the observed electrochemical responses.

During oxidation of LiFePO₄ and prior to the onset of O₂ evolution, the formation of CO₂ was observed. This CO₂ release may originate from (i) the oxidation of carbonaceous components—either the carbon coating on LiFePO₄ particles or the conductive additive (Super C65) (see Equation (1)^[12,13]) or (ii) the decomposition of residual Li₂CO₃ present on the surface of LiFePO₄ grains, as previously discussed in Part 1 of this study.^[14]



During the reduction of LiFePO₄, additional gas species—namely O₂, CH₄, and HF—were detected, the latter appearing just prior to the onset of H₂ evolution. The detection of O₂ at such low potential (≈2.7 V vs. Li⁺/Li) is unlikely to result from OER, suggesting alternative origins. One possible explanation is the decomposition of surface lithium carbonate, or the misidentification of gaseous species sharing the same mass-to-charge ratio (*m/z* = 32), such as SO₂ (confirmed by the simultaneous presence of its characteristic *m/z* = 64 signal). The latter could be originating from the counter electrode made of TiS₂ since when measuring TiS₂ as the working electrode, some SO₂ signal could be detected (see set-up Figure S1, Supporting Information).

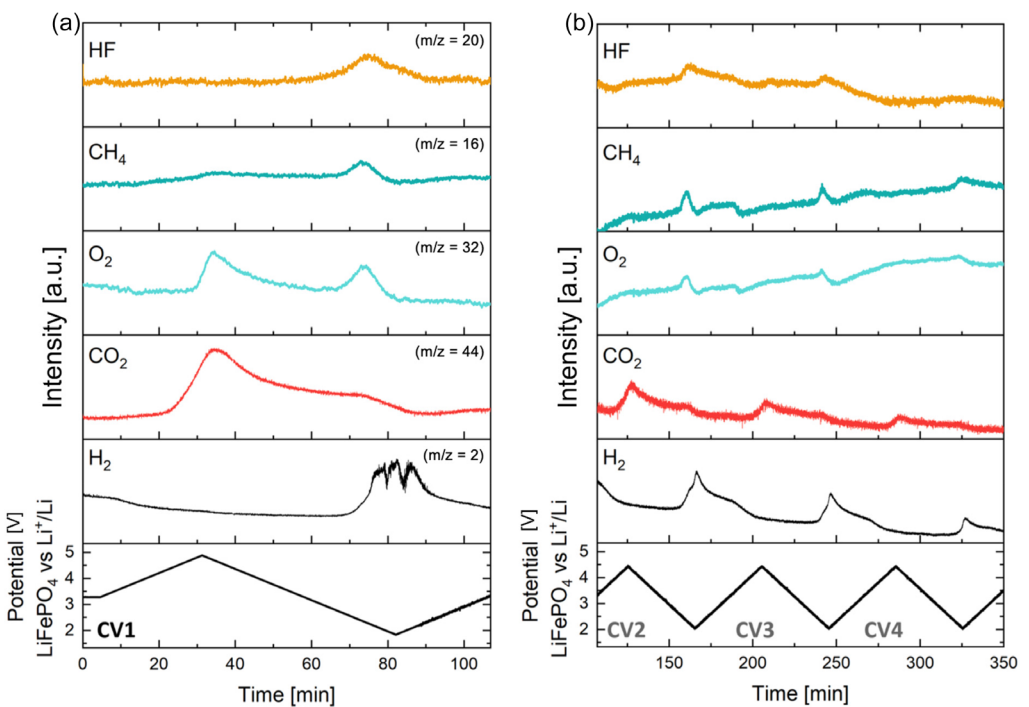


Figure 1. OEMS measurement during a) first CV cycle of LiFePO₄ and b) CVs second–fourth cycle of LiFePO₄ electrode performed at 1 mV s⁻¹ in 21 m LiTFSI solution under Ar-bubbling. The reference electrode is Ag/AgCl and the counter electrode is TiS₂.

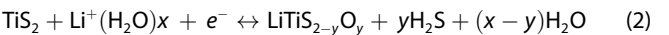
Due to the distance between the working electrode and the counter electrode as well as the quantity of the electrolyte use, it could take time from SO₂ gas to convert into O₂, which can send explain the lag time between the O₂ signal and the end of LiFePO₄ delithiation. Similarly, the origin of CH₄ remains ambiguous; it may either represent a true formation product (by hydrogenation/reduction of the carbon coating or conductive additive) or arise from fragmentation of other species with overlapping mass spectra. However, the synchronous evolution of O₂ and CH₄ signals suggests a common degradation pathway. HF formation is also observed and is likely associated with the decomposition of fluorinated species. In a fluorine-rich environment—stemming from both the binder and LiTFSI salt—combined with available protons (e.g., from water reduction), HF can form as a by-product. The presence of LiF on the LiFePO₄ surface during soaking and after cycling, as revealed by XPS analysis (see Figure 10)^[15] supports this hypothesis.

In subsequent CV cycles (Figure 1b), the voltage window was narrowed to between 4.45 and 2.1 V versus Li⁺/Li. This adjustment successfully suppressed O₂ evolution; however, a significant H₂ signal persisted, attributed to HER, involving residual free water in the electrolyte. CH₄ is also detected, and could result from the hydrogenation/reduction of the carbon coating or conductive additive, which is likely promoted by the generated H₂ from HER.

These initial observations reveal the occurrence of several parasitic processes—including carbon corrosion and hydrogenation/reduction, HER, and side reactions mimicking OER behavior—despite the electrodes operating within the expected ESW. Additionally, some degradation pathways remain insufficiently understood and warrant further investigation.

2.2. Case of TiS₂ Electrode Material

As previously discussed in Part 1^[14] of this study, TiS₂ undergoes chemical reactivity with the WISE during the soaking process, leading to observable gas evolution and the formation of a surface layer enriched in TiO₂. This gas release is hypothesized to originate from the formation of H₂S, resulting from the reaction of TiS₂ with water, as described by Equation (2).



By performing CV on TiS₂ electrode coupled to OEMS (Figure 2), we follow the evolution of H₂S and H₂.

Prior to the CV measurements, the H₂S signal remained stable and scarcely detectable. This observation is consistent with previous results obtained during soaking experiments, where TiS₂ was exposed to highly concentrated WISE. In this context, the limited availability of free water likely buffers the reaction between TiS₂ and the electrolyte (see Equation (2)). However, during electrochemical cycling and progressively decreasing the cell potential, a clear H₂S evolution is observed between 2.4 and 1.8 V versus Li⁺/Li, with a pronounced increase centered around 2.2 V versus Li⁺/Li. Interestingly, no H₂ gas is detected in this potential range, suggesting that H₂S evolution is not linked to the HER but rather arises exclusively from chemical interactions between TiS₂ and the remaining “free” water of the electrolyte as described in the following reference [16]. As previously reported during soaking experiments,^[14] TiS₂ develops a TiO₂-rich surface, indicative of high surface reactivity. At ≈2.2 V versus Li⁺/Li, lithium intercalation into the TiS₂ lattice occurs, leading to an

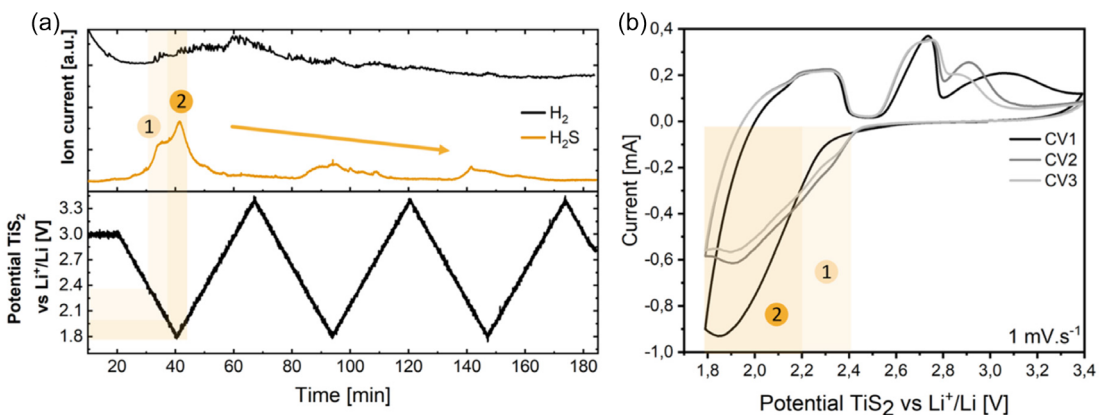


Figure 2. a) OEMS measurement of TiS_2 electrode material recorded at 1 mV s^{-1} in 21 m LiTFSI solution under Ar-bubbling. The reference electrode is Ag/AgCl and the counter electrode is LiFePO₄; (a) First three first CV cycles with corresponding H_2 ($m/z = 2$) and H_2S ($m/z = 34$) gas release, b) corresponding CV curves.

expansion of the *c*-axis.^[17] This structural change may facilitate the diffusion of electrolyte and residual water molecules into the interlayer space, promoting further H_2S evolution in accordance with Equation (2),^[16] as new reactive surfaces are exposed.

In subsequent CV cycles, the intensity of the H_2S signal significantly decreases and becomes nearly undetectable by the third cycle. This behavior may be attributed to (i) the formation of a passivating SEI that suppresses further surface reactions between protons and TiS_2 , and/or (ii) the complete transformation of the TiS_2 surface, through sulfur loss, into an inert TiO_2 layer. The latter hypothesis is supported by XPS data, which show that even prior to electrochemical cycling, the TiS_2 surface is largely converted into TiO_2 .^[14]

These findings indicate that both electroactive materials—LiFePO₄ and TiS_2 —exhibit chemical reactivity not only during electrochemical cycling but also at open-circuit voltage (OCV), as evidenced by the evolution of gaseous by-products. This highlights the intrinsic reactivity of the WISE with the electrode materials; that needs to be investigated in 3-electrode set-up, to deconvolute the evolution of the positive electrode from the negative electrode.

3. Three-Electrode Configuration Cell

The implementation of a reference electrode is essential to decouple the electrochemical behavior of the positive and negative electrodes. Owing to its well-defined and stable potential plateau in aqueous media, the LiFePO₄ electrode was selected as a pseudo-reference electrode in this study. The use of LiFePO₄ as a reference has been previously reported in the literature,^[18] however, several limitations must be acknowledged. These include (i) potential instability under varying temperature conditions,^[19,20] (ii) poor intrinsic electronic conductivity, which can lead to polarization effects that are dependent on the applied current density,^[21] and (iii) the requirement to partially delithiate the material in order to achieve a stable reference potential.

To accommodate these constraints, a three-electrode configuration based on a T-shaped Swagelok cell was employed (Figure S4, Supporting Information). This design ensures that the reference electrode remains in contact with the electrolyte without physically separating the working and counter electrodes, thereby minimizing cell resistance. Moreover, this setup enables *in situ* partial delithiation of the LiFePO₄ reference electrode, thereby avoiding external processing that could introduce contamination or experimental artifacts.

3.1. Electrochemical Performance

The cell was initially cycled at a low rate (C/5) for 15 cycles, using a cut-off voltage window of 0.5 V between LiFePO₄ and Li_xFePO_4 (black dots in Figure 3). The specific capacity recorded during the initial cycles slightly exceeded 170 mAh g⁻¹, indicating that LiFePO₄ undergoes nearly full and reversible lithiation/delithiation with additional side reactions, and a Coulombic efficiency above ≈98%. Nevertheless, a progressive capacity fading was observed, with a loss of 1.54 mAh g⁻¹ per cycle. This degradation is

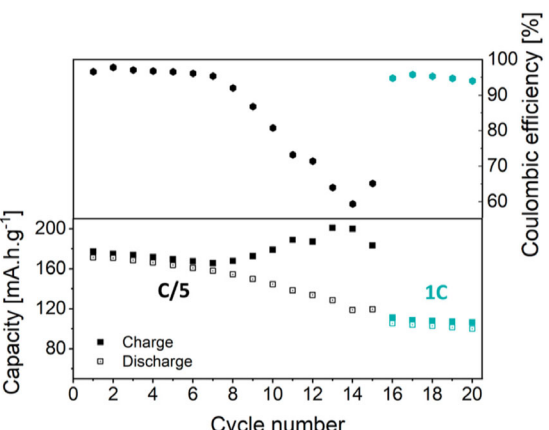


Figure 3. Coulombic efficiency and specific capacity of the three electrodes Swagelok cell cycling at various C-rates with different cycling protocols.

approximately thirty times higher than what has been previously observed in organic electrolyte systems under similar conditions in our laboratory, suggesting the presence of significant parasitic processes. To verify the effective delithiation of LiFePO₄ during cycling in WISE, *ex situ* X-ray absorption spectroscopy (XAS) measurements were carried out at the Fe K-edge. Five distinct cells were prepared corresponding to different states of charge (SOC): pristine, and at 20%, 40%, 60%, and 100% SOC and an additional one, being a chemically delithiated LiFePO₄. The experimental results are provided in Figure S5, Supporting Information and Note S1. Linear combination fitting of the XAS spectra, using reference spectra from stoichiometric LiFePO₄ and chemically delithiated FePO₄, enabled quantification of the Fe²⁺/Fe³⁺ ratio (Supporting Information, Note S2; Figure S6, S7, Supporting Information). The analysis revealed that the actual SOC from the structural state of the material was consistently lower than that estimated electrochemically—by a factor of 2.6 at 20% SOC and 1.2 at 100% SOC. These findings confirm that LiFePO₄ can indeed be delithiated in WISE; however, side reactions appear to interfere with the specific charge gathered. Indeed, it seems that a part of the obtained charges is only attributed to side reactions and not to the electrochemical reaction of LiFePO₄, which explains why the specific charge was higher than the theoretical one.

After the eighth cycle, the charge capacity began to increase continuously, reaching 200 mAh g⁻¹ by the twelfth cycle, whereas the discharge capacity steadily decreased, remaining below 160 mAh g⁻¹. After the 14th cycle, the cut-off potential (between LiFePO₄ and Li_xFePO₄) was reduced to 0.3 V versus Li_xFePO₄ (instead of 0.5 V used previously) which improves slightly the Coulombic efficiency (from 60% to 65%) without changing the specific capacity. Then, the cycling rate was set to 1C, resulting in drastic improvement of the Coulombic efficiency (reaching around 94%), meaning the cycling is much more reversible at high c-rate and the degradation reactions are buffered or at least, they have less time to settle. The important capacity decay (less than 110 mAh g⁻¹) means that more than a third of LiFePO₄ is either disconnected from the electronic network (carbon coating or carbon nanoparticles oxidized or leached by pH) and/or the particles are covered with a thick insulating passivation layer.

This divergence between charge and discharge capacity is indicative of parasitic reactions—most likely involving electrolyte degradation—which consume charge without contributing to reversible energy storage.

3.2. Voltage Profile of LiFePO₄ versus TiS₂

Voltage profile of LiFePO₄ versus TiS₂ is presented in Figure 4. As expected, LiFePO₄ exhibits a well-defined and stable potential plateau centered around 0 V versus Li_xFePO₄. During the initial cycles, this potential plateau remains highly stable, reflecting efficient, and reversible lithiation/delithiation processes. However, upon continued cycling, an additional oxidation feature emerges between ≈0.2 and 0.4 V versus Li_xFePO₄. This new feature is attributed to the onset of parasitic side reactions, which likely involve electrolyte degradation or interfacial instabilities.

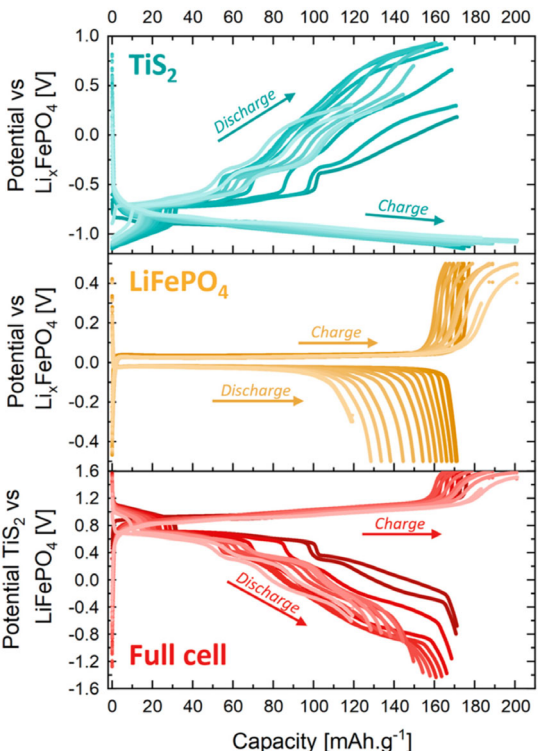


Figure 4. Potential profiles of the negative electrode (TiS₂, blue), the positive electrode (LiFePO₄, yellow), both referenced against Li_xFePO₄, as well as the full-cell voltage (red), recorded in a three-electrode Swagelok configuration cycled at a C/5 rate over 15 cycles. The color gradient represents the progression of cycles, with the darkest curve corresponding to the first cycle and the lightest to the fifteenth, allowing for a clear visualization of the electrochemical evolution with cycling.

Contrary to initial expectations, the pronounced irreversibility observed during cycling in this configuration does not appear to originate primarily from HER at the negative electrode—although this contribution cannot be entirely ruled out—but rather from parasitic processes occurring at the positive electrode. As suggested by the CV results (Figure 1), these processes could be associated with the evolution of CO₂ or O₂, or other degradation reactions. In the case of TiS₂, the lithiation process is characterized by a relatively stable potential plateau throughout cycling. In contrast, the delithiation process exhibits multiple potential plateaus that progressively diminish in length with each cycle, indicating a gradual loss of capacity and possible structural or interfacial degradation.

As seen, the cut-off potential of LiFePO₄, as well as the cycling rate can drastically influence the electrochemical performance of the cells. The next chapter is dedicated to the electrochemical performance of the cells LiFePO₄ versus TiS₂.

4. Influence of Electrochemical Parameters

4.1. Impact of the Cut-Off Potential

Based on previous literature reports,^[6,17] and electrochemical tests performed in organic electrolytes, the voltage window for

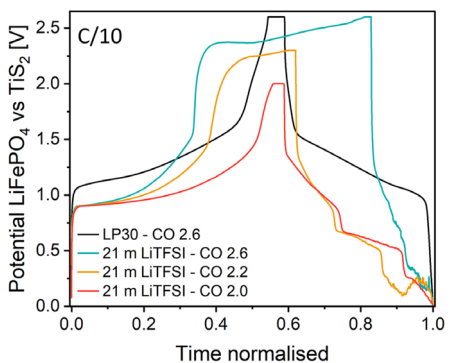


Figure 5. LiFePO₄ versus TiS₂ first cycle potential profile in LP30 (black), and 21 m LiTFSI solution at several cut-off potential. CO means cut-off (and is expressed in V).

LiFePO₄ versus TiS₂ full cells in WISE was set between 2.6 and 2.0 V. **Figure 5** displays the first galvanostatic cycle of a LiFePO₄ versus TiS₂ full cell in LP30 electrolyte, cycled with an upper cut-off voltage of 2.6 V, used here as a reference. These results are compared with those obtained under identical conditions in a 21 m LiTFSI aqueous electrolyte, with varying cut-off potentials. All measurements were conducted at a C/10 rate. Notably, the operating cell voltage in the aqueous system is \approx 250 mV lower than in the organic electrolyte, highlighting the influence of the electrolyte environment on the overall cell potential.

When the upper cut-off potential is set to 2.6 V, an additional voltage plateau emerges around 2.4 V, associated with a substantial charge consumption and pronounced irreversibility. This phenomenon is likely attributed to significant gas evolution within the cell, potentially resulting in electrolyte depletion and local pH fluctuations that adversely affect cell performance. Lowering the cut-off potential to 2.3 V mitigates gas generation, slightly improving the reversibility, although the voltage profile remains irregular—possibly due to local electronic disconnection phenomena. Further reduction of the cut-off potential to 2.0 V significantly enhances the electrochemical reversibility and appears to suppress gas evolution altogether. In this full-cell

configuration, gas release observed at the end of charge is most likely associated with HER at the negative electrode, suggesting that its potential drops below the ESW of the 21 m LiTFSI electrolyte.

4.2. Impact of the Cell Balancing

To evaluate the impact of electrode balancing on the electrochemical performance, two full-cell configurations were tested using a cut-off potential of 2.0 V: one in which the LiFePO₄ electrode is capacity-limiting, and another where both electrodes are balanced in terms of capacity. **Figure 6** presents the first-cycle potential profiles and the cycling performance of the LiFePO₄ versus TiS₂ full cells under both configurations. When the electrodes are balanced, the first-cycle Coulombic efficiency is significantly reduced, reaching only 52%, compared to 75% when LiFePO₄ is the limiting electrode. Furthermore, during prolonged cycling at a C/2 rate, the discharge capacity in the balanced configuration rapidly declines from 135 to 27 mAh g⁻¹, indicating poor cycling stability. In contrast, when LiFePO₄ is limiting, the specific capacity remains relatively stable, decreasing moderately from 118 to 92 mAh g⁻¹ over 30 cycles.

Regarding Coulombic efficiency, the trends differ markedly between the two configurations. For the LiFePO₄-limited cell, the Coulombic efficiency is initially high (>95%) but gradually decreases after the 15th cycle to reach \approx 80% by the 30th cycle. In the balanced configuration, the Coulombic efficiency shows erratic fluctuations, starting at around 80% and exhibiting irregular behaviour thereafter, suggesting the presence of unstable side reactions.

These findings highlight the importance of electrode balancing in preventing the potential excursion beyond the ESW, particularly the onset of the HER and OER. Despite its significance, this parameter is often overlooked in the literature on WISE, where an excess of positive electrode material is typically favored to compensate for lithium consumption during the formation of passivation layers. All subsequent experiments were conducted with LiFePO₄ as the capacity-limiting electrode to mitigate these parasitic effects.

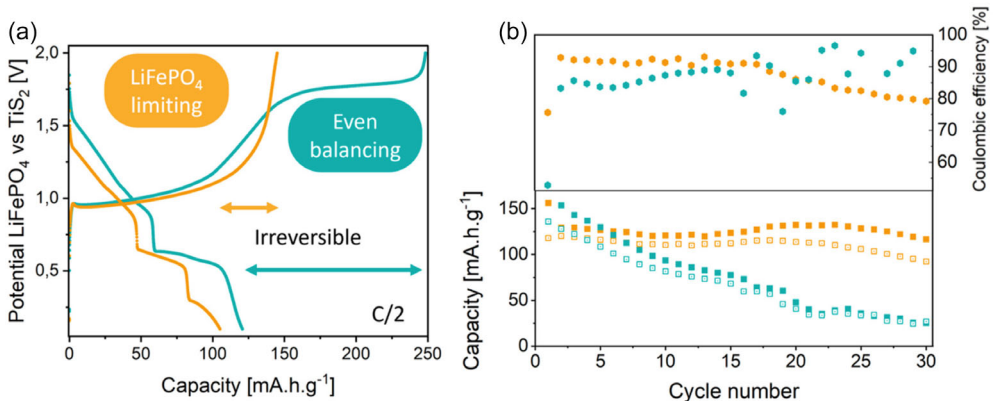


Figure 6. a) Potential profile along the first cycle of LiFePO₄ versus TiS₂ and b) specific capacity and Coulombic efficiency of LiFePO₄ versus TiS₂ cells in 21 m LiTFSI solution with 0.85 (yellow) and 1.3 (blue) mass balancing, corresponding respectively to 0.6 and 0.95 capacity balancing.

4.3. Impact of the Cycling Rate

Another critical parameter influencing the electrochemical performance of full cells employing WiSE is the applied C-rate. In the literature, relatively high C-rates are often employed to mitigate parasitic side reactions and to enable extended cycling. In this study, LiFePO₄ versus TiS₂ full cells were cycled at various C-rates ranging from C/10 to 1C to evaluate the rate-dependent behavior. At C/10, cell failure occurred after only a single cycle, highlighting the instability of the system under slow cycling conditions.

As shown in Figure 7a,b, both specific capacity and Coulombic efficiency are strongly affected by the C-rate. At C/5, the specific capacity is comparable to that observed in conventional organic electrolyte (LP30); however, the discharge capacity is significantly lower, leading to poor Coulombic efficiency. Across all cells cycled in 21 m LiTFSI, Coulombic efficiencies remained below 93%, suggesting the presence of persistent irreversible processes. These losses are likely attributed to continuous degradation mechanisms intrinsic to WiSE systems, including pH fluctuations, HER/OER, and the formation of passivation layers.

Nonetheless, an increase in the C-rate is associated with an improvement in Coulombic efficiency, particularly during the initial cycles. The C-rate also significantly influences cycling stability and overall cell lifetime. For instance, at a C/5 rate, the full cell was able to complete 15 cycles, whereas at higher rates (C/2 and 1C), the cells remained operational for over 30 cycles. However, such an interpretation should be nuanced by considering the effects of calendar aging. At C/5, one cycle requires ≈ 10 h (assuming no capacity loss), resulting in a total cycling duration of about 150 h after 15 cycles. In comparison, cells cycled at C/2 complete a cycle in roughly 4 h, thus reaching 30 cycles in ≈ 120 h. Therefore, the total aging time is comparable regardless of the C-rate applied. Over extended cycling, the cell operated at the highest C-rate (1C) exhibited the most stable electrochemical performance, with minimal variation in Coulombic efficiency up to 90 cycles. In contrast, the cell cycled at C/2 failed after 33 cycles, showing erratic Coulombic efficiency behavior. To compensate for any kinetics limitation, a 30 min potentiostatic step was introduced at the end of each charge and discharge. Figure 7c presents the evolution of the residual current during this

potentiostatic step. In full cells employing LP30 organic electrolyte, the residual current remained stable after each cycle. However, in WISE-based cells (21 m LiTFSI), the residual current increased over cycling, whereas it would be expected to decrease. This observation suggests that the potentiostatic step may promote parasitic reactions and degradation processes in aqueous media.

4.4. Long-Term Cycling Ability

Figure 8a presents the charge-discharge voltage profiles of the LiFePO₄ versus TiS₂ full cell cycled over 100 cycles at 1-C rate. Notably, the discharge curves exhibit distinct potential plateaus that are absent when cycling in conventional organic electrolytes, indicating the emergence of new electrochemical processes specific to the WISE environment.

Based on previous CV studies,^[6,17] these potential plateaus can be attributed to TiS₂ and reflect a biphasic reaction mechanism, in contrast to the solid-solution behavior typically observed in organic media. According to Zhang et al.,^[17] in aqueous electrolytes, the lithiation of TiS₂ proceeds via the formation of hydrated phases such as Li(H₂O)TiS₂ and Li(H₂O)₂TiS₂, which could be responsible for the observed voltage features. A comparable mechanism likely occurs in the highly concentrated 21 m LiTFSI electrolyte, despite the increased complexity of the lithium solvation structure due to significant anion participation.

To further elucidate the reaction mechanisms—particularly the evolution and eventual disappearance of the voltage plateaus during prolonged cycling—the differential capacity (dQ/dV) plots were calculated over the first 20 cycles and are displayed in Figure 8b.

After only three cycles, the discharge voltage plateau observed around 0.2 V progressively vanishes, suggesting the occurrence of irreversible processes. Similarly, the peak associated with the plateau near 0.5 V becomes progressively less intense, less defined and broader. This evolution likely reflects a structural amorphisation of the electrode material, which could lead to local heterogeneities in the electrochemical potential and result in broader, less distinct features in the differential capacity plots. Although the total charge exchanged (i.e., the area under the dQ/dV curve) may remain approximately constant, the process becomes increasingly disordered.

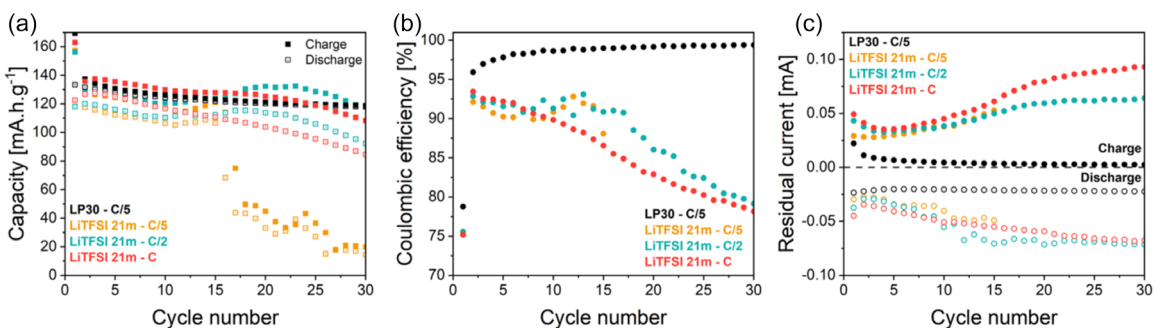


Figure 7. a) Specific charges of LiFePO₄ versus TiS₂ at different cycling rate, b) corresponding Coulombic efficiency, and c) residual current after 30 min potentiostatic step at various C-rate. The electrode mass balancing is 0.8, corresponding to 0.56 balancing in capacity based on theoretical specific capacity.

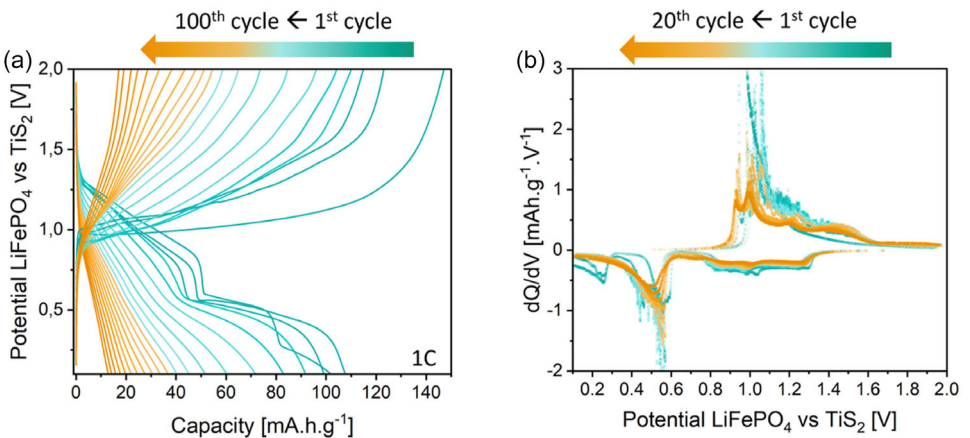


Figure 8. a) Potential profiles for the first 100 cycles of LiFePO₄ versus TiS₂. b) The corresponding differential capacity for 20 cycles in 21 m LiTFSI solution at 1-C rate and 2 V cut off potential. Electrode balancing is 0.8 in mass, corresponding to 0.56 balancing in capacity based on theoretical specific capacity.

On the charge side, the first cycle is characterized by a single prominent peak at \approx 1.0 V, corresponding to the delithiation of the LiFePO₄ electrode. However, with continued cycling, additional peaks emerge around 1.25, 1.00, and 0.95 V. The attribution of these new features could originate from the negative electrode. Indeed, in three-electrode measurement, we noticed additional processes on TiS₂ electrode (Figure 4) that could explain the new peaks seen previously in Figure 8b. Several factors may contribute to these observations, including structural amorphisation, altered water activity (e.g., Li⁺/H⁺ competition), pH-induced surface modifications (such as the leaching or degradation of the carbon coating on LiFePO₄), or other parasitic phenomena.

As demonstrated, multiple degradation processes occur during the cycling of cells in WISE. We initially investigated gas evolution reactions at both the positive and negative electrodes, highlighting their impact on the electrochemical performance over cycling. In the following section, we will focus on postmortem analyses to assess how these degradation processes affect the surface chemistry and morphology of both electrodes.

5. Surface and Interphases Investigation

Interphases play a critical role in the electrochemical performance of WISE systems, particularly at the negative electrode, where the formation of a SEI is essential to suppress HER. In this study, we investigate the formation and evolution of electrode/electrolyte interphases in LiFePO₄ versus TiS₂ full cells cycled in a 21 m LiTFSI aqueous electrolyte. The analysis is conducted using SEM and XPS. Both electrodes (LiFePO₄ and TiS₂) were characterized after the first charge at a 1C rate, with an electrode mass ratio of 0.85 (corresponding to a capacity ratio of 0.6), as well as at the end of the cell's lifetime (after \approx 60 cycles). To minimize residual salt contamination, all samples were gently rinsed prior to characterization, following a protocol previously established for soaked electrodes.^[14]

5.1. SEI Formation on TiS₂ Electrode

5.1.1. SEM Images

In the literature, the formation and composition of the SEI in aqueous electrolytes remain subjects of ongoing debate. To investigate its morphology using SEM, low-energy imaging (2 keV) was employed to minimize radiation damage to the electrode surface.^[22,23] Figure 9 presents SEM micrographs of a pristine TiS₂ electrode, an electrode after the first charge, and an electrode retrieved at the end of the cell's lifetime.

The pristine TiS₂ electrode (Figure 9a) exhibits a relatively clean surface, with particles of various sizes uniformly embedded within the binder and conductive carbon matrix. Following the first charge (at 1C rate, Figure 9b), the surface of the TiS₂ particles becomes partially covered with darker contrast features, which are attributed to the initial formation of the SEI, since at higher magnification they start to decompose. This interphase appears heterogeneous in distribution and preferentially localized on the active material particles rather than on the binder or conductive additives.

After extended cycling (Figure 9c), the surface morphology undergoes significant transformation. The active material particles are uniformly coated with a dense layer of nanoscale crystals like feature, \approx 100 nm in diameter, which were not observed after the first cycle. Additionally, larger and more prominent dark features, similar in appearance to those seen after the first charge, are also present.

5.1.2. XPS Measurements

The same electrodes were also observed by XPS. Figure 10 presents C1s, F1s, and O1s core level spectra for the three different samples showing several differences during cycling.

After the first charge, significant modifications are observed in the surface chemistry of the electrode, as evidenced by XPS analysis. On the C1s core-level spectrum (Figure 10a), the dominant signals initially assigned to C–C peak is less predominant

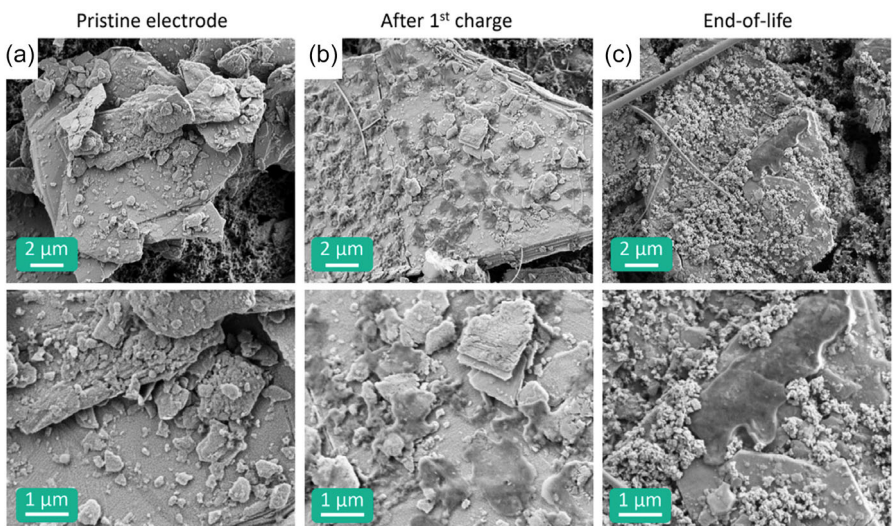


Figure 9. SEM images of TiS_2 electrodes a) pristine, b) after a first charge, and c) at end-of-life (cycled in full cell LiFePO_4 vs. TiS_2 in 21 m LiTFSI solution at 1C rate). Images were taken with two magnifications (5000X and 10000X) at 2 kV.

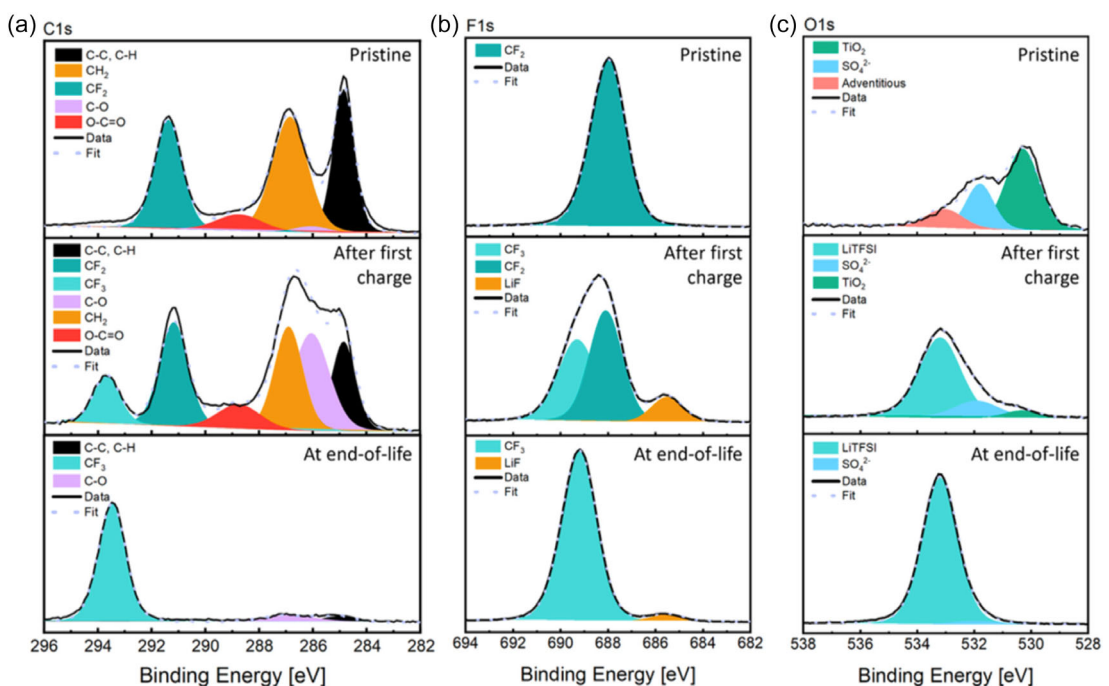


Figure 10. XPS core level spectra of a) C1s, b) F1s, and c) O1s of TiS_2 electrodes at pristine state, after a first charge and at end-of-life. Full cell of LiFePO_4 versus TiS_2 cycled in 21 m LiTFSI solution at 1C rate.

indicating that a surface layer is covering the electrode surface. The emergence of a CF_3 -related signal confirms the presence of LiTFSI salt on the electrode surface, despite rinsing the electrode. After prolonged cycling (end of life of the cell), only the signal attributed to CF_3 can be seen, indicating a surface layer higher than 10 nm (detection limits of our apparatus).

In the F1s spectrum (Figure 10b), the electrode displays strong contributions from both CF_3 and LiF species. The CF_3/LiF intensity ratio after the first charge is 31/17, whereas for the electrode merely soaked in 21 m LiTFSI (ref [14]), the ratio

was 41/5. Given the substantial LiF signal in the charged electrode, we can assume that the SEI is rich in LiF, already after a first charge. Upon prolonged cycling, LiF signal is barely detected since it is covered by salt residue leading to CF_3 signal. Based on SEM images, it seems that the crystal seen could be directly linked to the CF_3 salt residue.

In the O1s spectrum (Figure 10c), the postcharge signal is dominated by salt-related products, which hinders detailed interpretation of other oxygen-containing species. Still, this result can be linked to SEM image, where we saw that the dark layer was

preferentially covering the active materials, meaning that TiO_2 signal is barely visible. So, after only one charge, the sample is fully covered by decomposition products, mainly salt residue and LiF. At the end of cell life, the XPS spectrum is solely attributed to salt decomposition products, mainly $-\text{SO}_4^{2-}$ products. Looking at the N1s core level spectrum (Figure S8, Supporting Information), it confirms the presence of LiTFSI salt at the electrode surface, further supporting the hypothesis of crystallisation over cycling due to severe gas released observed previously.

Based on the SEM observations and XPS analyses, it appears that the initial stage of SEI formation on the TiS_2 electrode is predominantly characterized by the formation of LiF. This fluorinated interphase is, however, not uniformly distributed across the surface. As cycling progresses, regions initially coated with LiF persist—possibly with increased thickness—while the majority of the electrode surface becomes covered by precipitated LiTFSI salt and/or salt decomposition product. This salt accumulation is likely associated with electrolyte drying and water consumption during cycling, leading to salt crystallization at the electrode-electrolyte interface. Overall, the composition and evolution of the interphase observed here are consistent with the SEI formation mechanism previously proposed by Jommongkol et al.^[10]

5.2. SEI Formation on LiFePO_4 Electrode

5.2.1. SEM Images

As for the negative electrode, LiFePO_4 positive electrode was characterized after the first charge and at the end of cell life using SEM and XPS. Between the pristine state and after the first charge, SEM images (Figure 11a,b) reveal no significant morphological changes. The particles retain similar size and shape, and no apparent surface residues are observed, except the fibers from the separator.

However, after prolonged cycling, several notable changes are observed on the LiFePO_4 electrode (Figure 11c): (i) some particles appear to be fractured, likely due to mechanical stress induced by cycling and/or degradation of the carbon coating (gas released); (ii) the apparent quantity of LiFePO_4 particles seems reduced; and (iii) the binder and conductive carbon matrix becomes more visible. These findings suggest that LiFePO_4 electrode undergoes significant structural and morphological degradation during cycling. The fracture cannot be attributed to volume change since LiFePO_4 is known to have a very small volume change.

The observed morphological degradation may be attributed to fluctuations in pH and oxidative degradation of the carbon coating, which can induce particle cracking. Additionally, gas evolution during cycling could compromise the mechanical integrity of the electrode, potentially leading to the loss of electrical contact between the active material and the current collector. Surprisingly and contrary to the TiS_2 electrode, we do not visually see the presence of an organic layer type to be ascribed to the SEI formation. It could be that a crosstalk is occurring during cycling, leading to the dissolution of LiFePO_4 SEI covering up TiS_2 electrode.

5.2.2. XPS Measurements at Laboratory Scale

The same LiFePO_4 electrodes were further characterized by XPS, as shown in Figure 12. After the first charge, the spectra closely resemble those obtained for electrodes previously soaked in WISE electrolytes,^[14] with notable salt residues and an increased LiF signal (Figure 12b). The Fe2p core-level spectrum (Figure S9, Supporting Information) indicates that iron is predominantly in the Fe^{3+} oxidation state; however, complete oxidation is not achieved, as evidenced by comparison with the spectrum of a

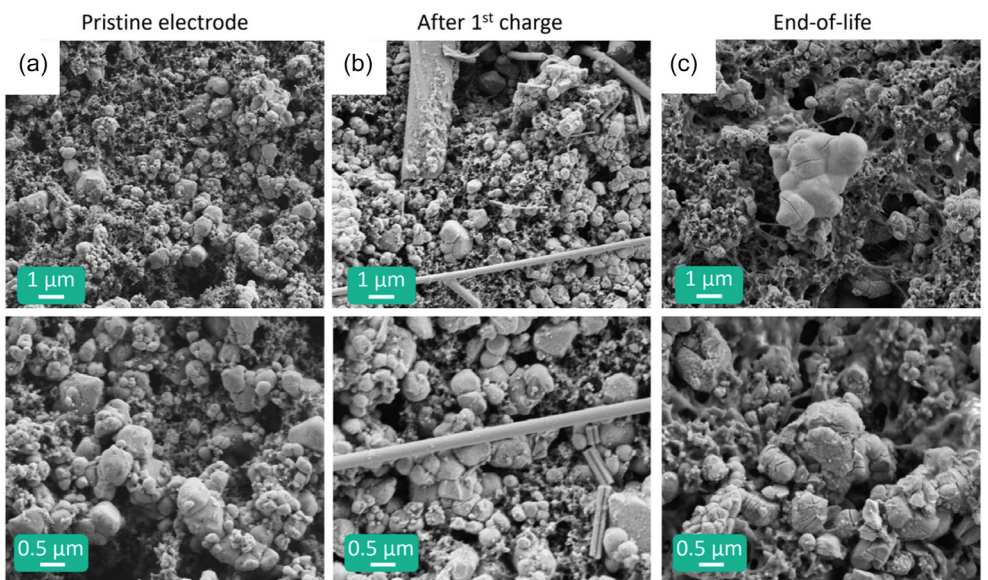


Figure 11. SEM images of LiFePO_4 electrodes a) pristine, b) after a first charge, and c) at end-of-life (cycled in full cell LiFePO_4 versus TiS_2 in 21 m LiTFSI solution at 1C rate).

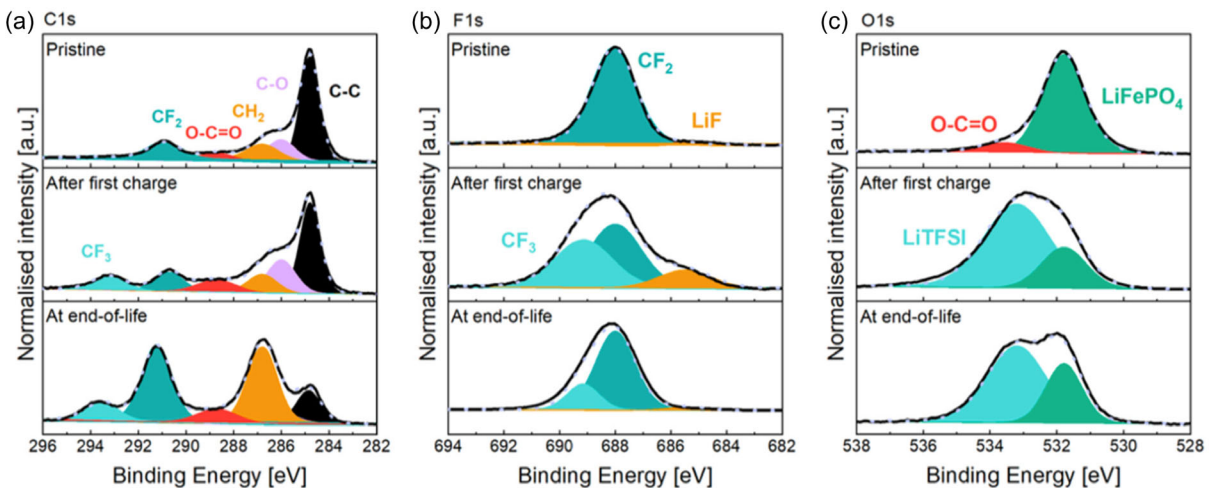


Figure 12. XPS core level spectrum of a) C1s, b) F1s, and c) O1s of LiFePO₄ electrodes at pristine state, and after a first charge and at end-of-life. Full cell of LiFePO₄ versus TiS₂ cycled in 21 m LiTFSI solution at 1C rate.

chemically delithiated LiFePO₄. This partial oxidation is consistent with the XAS at the Fe K-edge results presented in **Notes S1** and **S2**, as well as with electrochemical measurements showing that the specific charge delivered after a single charge exceeds the theoretical value—pointing toward ongoing parasitic or degradation processes. Overall, the surface degradation observed after one charge is relatively modest for LiFePO₄ and similar to that of electrodes soaked in WISE, in contrast to the more substantial changes seen for TiS₂.

At the end of the cell's life, the XPS spectra exhibit significant differences compared to those obtained after the first charge. The C1s core-level spectrum (Figure 12a) is now dominated by signals attributed to the binder, with prominent CF₂ and CH₂ contributions at 291.2 and 286.8 eV, respectively, while the C–C peak at 284.8 eV has decreased in intensity. This attenuation of the C–C signal may be explained by three hypotheses: (i) the formation of a surface layer during cycling that attenuates the signal from C–C bound signal; (ii) electrochemical degradation or corrosion of conductive carbon nanoparticles, as suggested by DEMS, reducing their contribution; and/or (iii) leaching or oxidation of the carbon coating on LiFePO₄ particles, potentially driven by pH fluctuations, as seen from SEM observations of particle cracking.

In the F1s core-level spectrum (Figure 12b), the presence of CF₂ (from the binder) and CF₃ (from the salt) remains evident, while the LiF signal vanished. This could indicate compositional changes at the electrode surface, with an apparent increase in binder content—consistent with SEM images showing a reduced presence of LiFePO₄ particles—and/or the possible leaching of LiF via cross-talk phenomena. These features corroborate the SEM findings, where prolonged cycling led to noticeable morphological changes and a decrease in the apparent abundance of LiFePO₄ on the surface.

In the O1s spectrum (Figure 12c), the LiFePO₄ contribution is more prominent than after the first charge, suggesting that after extended cycling, the binder and conductive agents may have

been depleted or displaced from the surface, exposing more of the active material.

To gain further insight, hard X-ray photoelectron spectroscopy (HAXPES) measurements were performed at the GALAXIES beamline (SOLEIL synchrotron). However, the end-of-cell-life samples exhibited significant beam damage and severe charging effects under synchrotron radiation, limiting the interpretability of the data.

5.2.3. XPS Measurements at Large Scale Facilities (GALAXIES Beamline at SOLEIL)

The sample analyzed after a single charge is presented in **Figure 13**. Three different incident photon energies were employed, allowing the investigation of different sampling depths. The first energy (3 keV) probes approximately twice as deep as conventional laboratory-based XPS. At this depth, the core-level spectra largely resemble those obtained via laboratory XPS, except for the F1s core-level spectrum (Figure 13b). The LiF signal is significantly attenuated in the HAXPES spectrum, which may be attributed to two possible explanations: (i) the LiF layer is thinner than ≈ 20 nm, and/or (ii) the interaction of the beam with the salt differs from that observed under laboratory conditions. Based on the beam sensitivity evaluations conducted at the GALAXIES beamline, the second hypothesis can be reasonably excluded. Consequently, it is most likely that the LiF layer formed during the first charge is thinner than 20 nm.

At greater depths (i.e., with higher photon energies and thus longer inelastic mean free paths), the contributions from the different core-level spectra attributed to the salt components progressively diminish and become nearly undetectable beyond a depth of ≈ 65 nm. At this point, the features closely resemble those of the pristine electrode, suggesting that most of the chemical degradation processes are confined to the near-surface region of the electrode.

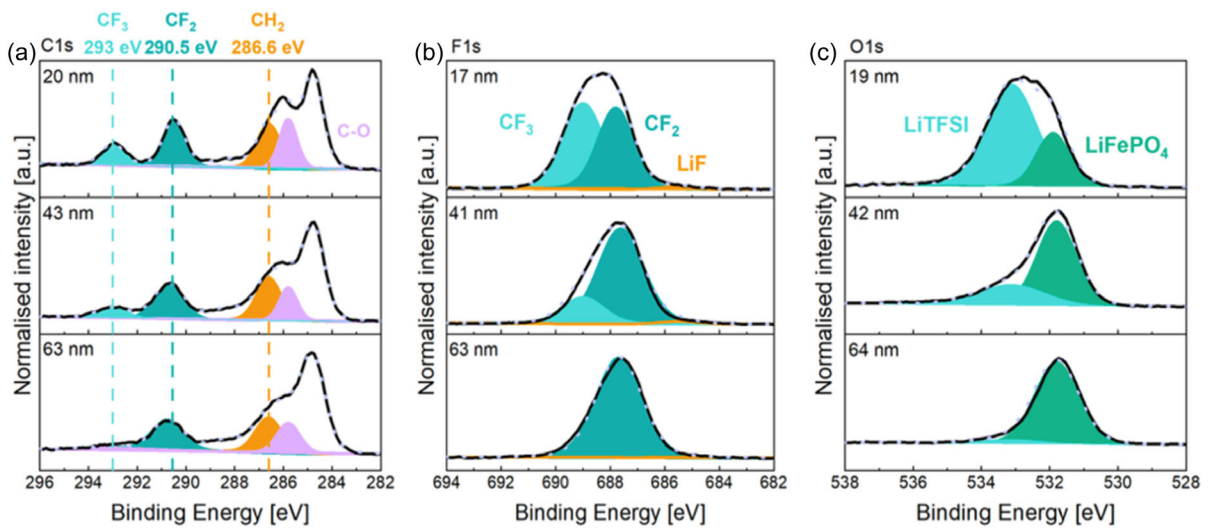


Figure 13. XPS core level spectrum (collected at GALAXIES beamline) of a) C1s, b) F1s, and c) O1s obtained from LiFePO₄ electrodes after the first charge in full cell LiFePO₄ versus TiS₂ cycled in 21 M LiTFSI solution at 1C rate at three different energies, 3, 6.9, and 11 keV.

6. Conclusion

This work provides a comprehensive analysis of the degradation mechanisms occurring in LiFePO₄ versus TiS₂ full cells cycled in highly concentrated aqueous electrolytes (21 M LiTFSI). Through a combination of OEMS, SEM, XPS, and HAXPES techniques, we demonstrate that both electrodes, despite being electrochemically stable within the theoretical ESW, experience significant side reactions that contribute to capacity fading and poor Coulombic efficiency. In particular, TiS₂ exhibits surface reactivity leading to H₂S evolution and TiO₂ formation, while LiFePO₄ suffers from morphological degradation, carbon corrosion, and passivation phenomena. The formation of a LiF-based SEI is confirmed but remains heterogeneous and unstable over cycling, giving way to the precipitation of salt residues that further hinder electrode performance. Our results also underline the pivotal role of cycling rate, voltage cut-off, and electrode balancing in modulating these degradation pathways. Faster cycling improves reversibility by suppressing parasitic reactions, while careful balancing prevents potential excursions that lead to HER/OER. Overall, this study highlights the intrinsic limitations of WiSE systems and emphasizes the necessity for deeper mechanistic understanding and proper cell engineering to unlock their full potential for practical applications.

7. Experimental Section

OEMS

The three-electrode OEMS set-up allows to use a small amount of electrolyte (below 15 mL); the processes can be discriminated between the positive and the negative electrode (Figure S1, Supporting Information). To prevent the liquid electrolyte from being sucked in by the vacuum, three PTFE membranes (PF-002H, Cobetter filtration, 20 µm thick, 20 nm diameter pores) were positioned on top

of the stainless-steel frit. The pore size allows gas permeability but remains small enough to be impermeable to the liquid electrolyte. The working electrode used in this configuration was self-standing to allow gas and electrolyte flow in the electrode porosity. The current was transported through a stainless-steel grid on top of the electrode surface and linked to a gold wire for electrical connection. To monitor properly the potential during the experiment, an Ag/AgCl reference electrode in a solution of 3 mol L⁻¹ NaCl is placed in the electrolyte solution and argon is permanently bubbling in the solution to prevent dissolved O₂ to interfere during the measurement. The gas produced at the measured electrode are directly driven thanks to vacuum to the mass spectrometer (QMG 220, Pfeiffer Vacuum). A strong electric field ionized the incoming species and then a magnetic field (Lorentz force) leads them toward the mass spectrometer sensor. The deflection undergone by the species depends directly on the ratio between its molar mass *m* and its charge *z* that is defined as the electric charge of the ion formed after ionization, corresponding to the number of electrons removed from the species. Thus, by selecting the appropriate *m/z* ratio, it is possible to choose which species will be directed to the detector.

ESW

As Li metal cannot be used as counter and reference electrode in WiSE, the measurement was performed in full-cell configuration with the other electrodes material (in the present case TiS₂) being the counter electrode deposited on stainless steel mesh, used as current collector, and a gold wire was attached to the stainless-steel mesh (scheme of the electrochemical cell is given in Figure S1, Supporting Information).

Three Electrode Cells—Reference

The size of the reference electrode was minimized to 4 mm diameter, which delivers a specific capacity of 0.06 mAh. To ensure that LiFePO₄ (working electrode) is still the limiting electrode, its capacity was set to deliver 0.21 mAh, and the negative electrode, TiS₂, was dimensioned to deliver a capacity of 0.57 mAh. At the end, the 3-electrode cell has a capacity balancing around 0.4.

Electrolyte Preparation

Lithium bis(trifluoromethanesulfonyl)imide (LiTFSI, LiN(SO₂CF₃)₂) was purchased from Solvionic and stored in an Ar-filled glovebox. LiTFSI electrolyte solutions of 21 m was prepared by mixing LiTFSI salt and Milli-Q ultrapure water. For comparison, LP30 organic electrolyte (1 M LiPF₆ in EC/DMC 1:1) (Solvionic, France) was used also.

Electrode Elaboration

Two electrode formulations were used in this paper: one for electrodes on current collector and one for self-supported electrodes. Composite electrodes were obtained by mixing 80 wt% of active materials (LiFePO₄ (LFP, MTI supplier) or TiS₂ (Sigma Aldrich, France) as active material), 10 wt% of carbon super C65 (Imerys), and 10 wt% of poly(vinylidene fluoride) (PVdF-kynar 900HSV, Arkema). The powders are grinded altogether by hand for at least 10 min prior adding then *N*-methylpyrrolidone (NMP) to solubilize the binder. The as-obtained slurry is then casted onto an aluminum foil, used as a current collector, by a doctor blade technique. The electrodes are then dried at 70 °C for 8 h. Once dried, the electrodes are punched in 12 mm diameter disk with an active material loading around 2.5 mg cm⁻². The porosity of the electrodes was estimated to be around 60%.

For self-supported electrodes, the ratio are 70%wt of active material, 10%wt of carbon super C65 and 20%wt PVDF-kynar Flex 2751–00 (Arkema). The powders were ground altogether in acetone to solubilize the binder to form a slurry. The slurry is then casted onto a glass plate by a doctor blade technique with wetted thickness between 150 and 250 µm. The electrodes are then dried at 70 °C for 8 h.

Regarding the balancing electrochemical test, the mass ration between LiFePO₄ electrode and TiS₂ is 0.85, meaning that if we consider the theoretical capacity of both materials, the capacity balancing is around 0.6, with LiFePO₄ electrode being the limiting electrode.

Chemical Delithiation of LiFePO₄

To obtain a reference of delithiated LiFePO₄, we were inspired by the chemical delithiation protocols in the literature.^[24,25] 500 mg of LiFePO₄ are immersed in 12.5 mL of 0.5 mol L⁻¹ solution of NO₂BF₄ acetonitrile for 24 h under magnetic stirring in a controlled atmosphere (Ar-glovebox). The powders are then rinsed with acetonitrile four times before being dried at 120 °C in a Buchi oven.

Cycling Tests

Coin cells are assembled in an Ar filled glovebox. Before cell assembly, the electrodes and the glass fiber separator (Whatman) are dried at 130 °C under dynamic vacuum. LiFePO₄ and TiS₂ composite electrodes are used as positive electrode, a glass-fiber separator is soaked with LP30 electrolyte 1/1 wt/wt dimethyl carbonate (DMC)/ ethylene carbonate (EC) and 1 M LiPF₆ (Solvionic), and lithium metal is used as counter electrode. The half cells are cycled at 25 °C in a temperature-controlled oven using galvanostatic cycling with potential limitation (G CPL) between 2.8 and 4 V versus Li⁺/Li at a C/10 rate. Along the manuscript all the potential are expressed against Li metal counter electrode meaning versus Li⁺/Li.

XPS Measurements

XPS spectra were obtained using a Thermo Scientific K-alpha spectrometer with a monochromated Al X-ray source (1486.6 eV, spot size 400 µm, constant angle of 90° between the sample surface and the analyzer). Pass energies of 30 and 100 eV were employed to record the core level and survey spectra, respectively. All spectra were acquired using an electron flood gun to compensate for possible positive charge accumulation during measurements. The obtained spectra are then deconvoluted and fitted using CasaXPS software with the Tougaard background type and calibrated using the C-C bound at 284.8 eV.^[26]

XAS Measurements

The XAS measurements of iron K-edge were performed at the ID21 beamline^[27] at ESRF. The beam was focused to 0.4 × 0.9 µm² with a Kirkpatrick-Baez mirror system. The energy selection was done using a double crystal fixed exit monochromator equipped with Si 111 crystals. Energy calibration was done using an Fe foil by taking the maximum of the first peak of the first derivative spectrum (7.112 keV). XANES spectra in selected points of interest were measured at the Fe K-edge (0.5 eV step and 100 ms dwell time per energy step). This beamline allows the acquisition of absorption spectra in fluorescence and in transmission, for this study only spectra in transmission were analyzed. The incoming intensity (I₀) and the transmission intensity (I_t) were recorded using Si photodiodes. Data were processed using PyMCA software.^[28] First, intensity variations due to synchrotron electron injection were corrected in all raw data. Individual XANES spectra were processed using Orange software^[29] with the spectroscopy add-on.^[30]

HAXPES

HAXPES measurements were performed at GALAXIES beamline at SOLEIL synchrotron, using a EW4000 Scienta hemispherical electron analyzer oriented at 90° to the incident photon beam.^[31,32] The pressure inside the chamber is in the range of 10⁻⁹ mbar. The beamline energy is tuned by adjusting the Bragg angle of the cryogenically cooled double-crystal Si 111 monochromator (DCM). The first order reflexion of the DCM was used for the 3.0 keV photon energy, the third order was used for 6.9 and 11 keV photon energy. The resolution is between 300 and 360 meV depending on the photon energy. The photon beam (30 × 575 µm) incidence is 10° with the sample surface.

Acknowledgements

C.D. is grateful for the financial support provided by the IDEX project from the Université Grenoble Alpes. This research has benefited from the characterization equipment of the Grenoble INP-CMTC platform support by the Center of Excellence of Multifunctional Architectured Materials "CEMAM" (grant ANR-10-LABX-44-01) funded by "Investments for the Future Program." Beamtime at the ESRF, ID21 beamline was granted within the Battery Pilot Hub MA4929 "Multi-scale Multi-techniques investigations of Li-ion batteries: toward a European Battery Hub". The authors acknowledge SOLEIL Synchrotron for provision of beamtime at the GALAXIES beamline under the proposal number 20231865.

Conflict of Interest

The authors declare no conflict of interest.

Data Availability Statement

The data that support the findings of this study are available from the corresponding author upon reasonable request.

Keywords: electrochemical properties · gas analyses · hydrogen evolution reaction and oxygen evolution reaction · water-in-salt electrolytes · X-ray photoelectron spectroscopy

- [1] D. Dong, C.-X. Zhao, X. Zhang, C. Wang, *Adv. Mater.* **2025**, 2418700.
- [2] D. G. Vazquez, J. Ingenmey, K. Trapp, D. Ciliak, M. Salanne, M. R. Lukatskaya, *J. Am. Chem. Soc.* **2025**, 147, 35953.
- [3] L. Suo, O. Borodin, T. Gao, M. Olguin, J. Ho, X. Fan, C. Luo, C. Wang, K. Xu, *Science* **2015**, 350, 938.
- [4] L. Suo, F. Han, X. Fan, H. Liu, K. Xu, C. Wang, *J. Mater. Chem. A* **2016**, 4, 6639.
- [5] F. Wang, L. Suo, Y. Liang, C. Yang, F. Han, T. Gao, W. Sun, C. Wang, *Adv. Energy Mater.* **2017**, 7, 1600922.
- [6] W. Sun, L. Suo, F. Wang, N. Eidson, C. Yang, F. Han, Z. Ma, T. Gao, M. Zhu, C. Wang, *Electrochim. Commun.* **2017**, 82, 71.
- [7] W. G. Kidanu, T. N. Vo, S. So, J. Hur, I. T. Kim, *Appl. Surf. Sci.* **2021**, 553, 149496.
- [8] L. Droguet, A. Grimaud, O. Fontaine, J.-M. Tarascon, *Adv. Energy Mater.* **2020**, 10, 2002440.
- [9] J. Xie, D. Lin, H. Lei, S. Wu, J. Li, W. Mai, P. Wang, G. Hong, W. Zhang, *Adv. Mater.* **2024**, 36, 2306508.
- [10] R. Jommongkol, S. Deebansok, J. Deng, Y. Zhu, R. Bouchal, O. Fontaine, *Small* **2024**, 20, 2303945.
- [11] L. Droguet, M. Courty, O. Fontaine, J. M. Tarascon, A. Grimaud, *J. Electrochim. Soc.* **2022**, 169, 070510.
- [12] L. Zhang, C. Zhang, E. J. Berg, *Adv. Mater.* **2025**, 37, 2407852.
- [13] J. Zhao, Z. Tu, S. H. Chan, *J. Power Sources* **2021**, 488, 229434.
- [14] O. K. Célia Doublet, M. Mirolo, J. Drnec, V. Martin, E. Suard, L. L. S. Lorenzo, C. Villevieille, *Batteries Supercaps* **2025**, e202500539.
- [15] X. Hou, L. Zhang, N. Gogoi, K. Edström, E. J. Berg, *Small* **2024**, 20, 2308577.
- [16] L. Zhang, X. Hou, K. Edström, E. J. Berg, *Batteries Supercaps* **2022**, 5, e202200336.
- [17] L. Zhang, F. Kühlung, A.-M. Mattsson, L. Knijff, X. Hou, G. Ek, T. Dufils, F. H. Gjørup, I. Kantor, C. Zhang, W. R. Brant, K. Edström, E. J. Berg, *ACS Energy Lett.* **2024**, 9, 959.
- [18] F. La Mantia, C. D. Wessells, H. D. Deshazer, Y. Cui, *Electrochim. Commun.* **2013**, 31, 141.
- [19] Z. Ahmed, A. J. Roberts, T. Amietszajew, *Energy Technol.* **2022**, 10, 2200248.
- [20] Y. Xiao, R. Xu, C. Yan, J.-Q. Huang, Q. Zhang, M. Ouyang, *Adv. Funct. Mater.* **2022**, 32, 2108449.
- [21] R. Raccichini, M. Amores, G. Hinds, *Batteries* **2019**, 5, 12.
- [22] C. Villevieille, *Nat. Nanotechnol.* **2025**, 20, 2.
- [23] S. F. Mayer, M. Mirolo, A. A. I. Velez, O. Korjus, E. Suard, L. Lecarme, J.-B. Ducros, C. Villevieille, *Small Struct.* **2024**, 5, 2400225.
- [24] H.-W. Hsieh, C.-H. Wang, A.-F. Huang, W.-N. Su, B. J. Hwang, *Chem. Eng. J.* **2021**, 418, 129191.
- [25] X.-J. Wang, H.-Y. Chen, X. Yu, L. Wu, K.-W. Nam, J. Bai, H. Li, X. Huang, X.-Q. Yang, *Chem. Commun.* **2011**, 47, 7170.
- [26] N. Fairley, V. Fernandez, M. Richard-Plouet, C. Guillot-Deudon, J. Walton, E. Smith, D. Flahaut, M. Greiner, M. Biesinger, S. Tougaard, D. Morgan, J. Baltrusaitis, *Appl. Surf. Sci. Adv.* **2021**, 5, 100112.
- [27] M. Cotte, E. Pouyet, M. Salomé, C. Rivard, W. De Nolf, H. Castillo-Michel, T. Fabris, L. Monico, K. Janssens, T. Wang, P. Sciau, L. Verger, L. Cormier, O. Dargaud, E. Brun, D. Bugnatz, B. Fayard, B. Hesse, A. E. P. del Real, G. Veronesi, J. Langlois, N. Balcar, Y. Vandenberghe, V. A. Solé, J. Kieffer, R. Barrett, C. Cohen, C. Cornu, R. Baker, E. Gagliardini, et al., *J. Anal. At. Spectrom.* **2017**, 32, 477.
- [28] V. A. Solé, E. Papillon, M. Cotte, P. Walter, J. Susini, *Spectrochim. Acta, Part B* **2007**, 62, 63.
- [29] J. Demšar, T. Čurk, A. Erjavec, Č. Gorup, T. Hočevar, M. Milutinovič, M. Možina, M. Polajnar, M. Toplak, A. Starič, M. Štajdohar, L. Umek, L. Žagar, J. Žbontar, M. Žitnik, B. Zupan, *J. Mach. Learn. Res.* **2013**, 14, 2349.
- [30] M. Toplak, G. Birarda, S. Read, C. Sandt, S. M. Rosendahl, L. Vaccari, J. Demšar, F. Borondics, *Synchrotron Radiat. News* **2017**, 30, 40.
- [31] D. Céolin, J. M. Ablett, D. Prieur, T. Moreno, J. P. Rueff, T. Marchenko, L. Journel, R. Guillemin, B. Pilette, T. Marin, M. Simon, *J. Electron Spectrosc. Relat. Phenom.* **2013**, 190, 188.
- [32] J. P. Rueff, J. M. Ablett, D. Céolin, D. Prieur, T. Moreno, V. Balédent, B. Lassalle-Kaiser, J. E. Rault, M. Simon, A. Shukla, *J. Synchrotron Radiat.* **2015**, 22, 175.

Manuscript received: August 29, 2025

Revised manuscript received: October 17, 2025

Version of record online: